A Multi-Output Modular Wireless Power Transfer System With Constant-Current Characteristic

Wenxuan Pan, Rongbin Liu, Ronghuan Xie, *Graduate Student Member, IEEE*, Yizhan Zhuang, *Member, IEEE*, Xingkui Mao, *Member, IEEE*, and Yiming Zhang, *Senior Member, IEEE*

***Abstract*—In the medium- and high-capacity power applications, typically multiple switches connected in series and parallel are used in power electronic converters to handle high voltages and currents. Powering the driving circuits and auxiliary units with high insulation requirements is challenging. This article proposes a modular multioutput wireless power transfer system with constant-current (CC) output characteristics for auxiliary power supply. Compared with conventional solutions, there is no need for complex control circuits and much magnetic material. The dual-frequency topology with CC outputs is derived by applying the analytical method that used to obtain the dual-frequency topology with constant-voltage (CV) outputs. The conditions for the system to maintain zero phase angle at different frequencies are discussed. Lower output fluctuations than single-frequency multioutput systems and dual-frequency CV output systems are verified. A magnetic coupler with integrated compensation inductors is designed to eliminate the need for discrete inductors and improve the power density. An experimental prototype is built to verify the validity of the theory. The WPT system achieves an output current fluctuation of no more than 4.78%, a maximum system efficiency higher than 85%, and an output power of more than 10 W at a single port, which can well meet the requirements of auxiliary power supply.**

***Index Terms*—Auxiliary power supply (APS), constant-current (CC), dual frequency, modularity, wireless power transfer (WPT).**

I. Introduction

WIRELESS power transfer (WPT) is an emerging energy transmission method that offers advantages in improving reliability, safety, convenience, and equipment longevity [1], [2], [3], [4], [5]. Nowadays, WPT is widely employed in underwater applications, consumer electronics, electric vehicles, rail transit, implanted medical devices, etc. [6], [7], [8], [9], [10]. The transmission mechanism of WPT is similar to that of transformers; hence, it is also known as a coreless transformer. Because of the air gap, WPT has high insulation capability and can be used in medium- and high-capacity power conversion applications [11], [12].

In medium-voltage dc distribution grids and high-voltage direct-current transmission, a modular design is adopted in power electronic converters to cope with high voltage and current stresses, such as modular multilevel converters, high-voltage dc circuit breakers, solid-state transformers, and so on. Since each submodule has a different potential, galvanic isolation needs to be established between the auxiliary power supplies. A conventional solution is the dc–dc step-down converter, which obtains the electric power from the local medium voltage dc link. However, the significant voltage difference requires high insulation capability, increasing the difficulty and cost of transformer design. Another solution is to use an external power supply. It offers better reliability and lower insulation requirements. Most designs utilize magnetic coupling to provide galvanic isolation, such as multiple magnetic rings.

The WPT technology can provide a flexible, reliable, and effective solution for auxiliary power supply. Compared with conventional solutions, there is no need for complex control circuits and much magnetic material. In practice, submodules of a power converter are integrated into the cabinet and can be stacked horizontally or vertically, as shown in Fig. 1(a). The domino WPT system is highly compatible with this placement. In a domino-type WPT system, each relay coil acts as a receiving and transmitting coil while supplying power to the local load [13]. It provides galvanic isolation for outputs and enables power supply over long distances. A capacitively tuned relay WPT system was proposed in [14]. Different power distributions at variable loads and distances can be satisfied by changing the capacitance. Besides the driving circuit, a submodule contains controllers, sensors, etc., which have different voltage levels. The class-E inverter topology is improved to boasts dual outputs with only one power switch thanks to its series and parallel resonant cavities [15]. Half-wave rectifiers and a synchronous rectifier were utilized to realize multiple output channels [16]. The rectifier was improved to integrate with the buck converter, and $4 + n$ semiconductor devices and n inductors are utilized to achieve $1 + n$ output channels [17]. Although the above studies achieve outputs of different voltage levels but on condition of complex control mechanisms. For better performance, two-stage auxiliary power supplies are used more often. The first stage converter handles the insulation voltage without feedback control and the second stage converters regulate the outputs, as shown in Fig. 1(b).

Received 10 July 2024; revised 28 September 2024 and 4 November 2024; accepted 30 November 2024. Date of publication 9 December 2024; date of current version 28 January 2025. This work was supported in part by the National Natural Science Foundation of China under Grant 52107183 and in part by the Natural Science Foundation of Fujian Province under Grant 2022J06011. Recommended for publication by Associate Editor J. Acero. *(Corresponding authors: Yiming Zhang; Yizhan Zhuang.)*

The authors are with the Fujian Engineering Research Center of High Energy Batteries and New Energy Equipment & Systems, School of Electrical Engineering and Automation, Fuzhou University, Fuzhou 350108, China (e-mail: 220120033@fzu.edu.cn; 220127070@fzu.edu.cn; 230127018@fzu.edu.cn; zyz_joe@fzu.edu.cn; mxk782@fzu.edu.cn; zym@fzu.edu.cn).

Color versions of one or more figures in this article are available at https://doi.org/10.1109/TPEL.2024.3512656.

Digital Object Identifier 10.1109/TPEL.2024.3512656

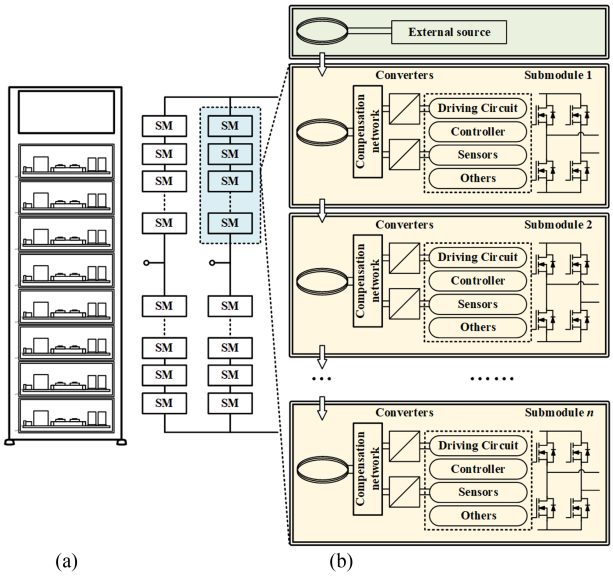

Fig. 1. Application of modular multioutput WPT system. (a) Placement of submodules in practice. (b) System configurations of domino-type WPT system for auxiliary power supply.

In the driving circuit, the driving resistance is usually altered to shorten the switching delay time, reduce the switching loss, etc., to achieve excellent switching performance. As a result, the outputs of the domino system change, and the interconnection of load powers adds complexity to power management. A domino system with load-independent outputs is preferable. Considering the usage of second stage converters, both constant-current (CC) and constant-voltage (CV) outputs are acceptable. However, the ideal load-independent outputs cannot be realized due to the presence of parasitic resistance. A bilateral excitation scheme for a domino-type WPT system was proposed to reduce output fluctuations and improve system reliability, but additional inverters require synchronized control [18]. For multiple second-stage converters connected to the same output port of first-stage converter, all second-stage converters are affected when the input impedance of one converter varies. A multi-frequency system can be used to solve this problem [19]. Higher order compensation networks are used to construct a multi-frequency resonant WPT system that enables selective distribution of load power [20]. By combining the multi-frequency resonant topology with the domino WPT system, a domino WPT system with lower output fluctuations can be obtained [21].

This article proposes a modular dual-frequency WPT system with multiple CC outputs. Section II presents the principle of circuit topology to realize dual-frequency CC characteristics. Section III analyzes the output characteristics. In Section IV, the magnetic couplers are designed. The effectiveness of the proposed system is experimentally verified in Section V. Finally, Section VI concludes the article.

II. Proposed Multioutput System

The proposed modular dual-frequency topology with multiple CC outputs is shown in Fig. 2. The system can be divided

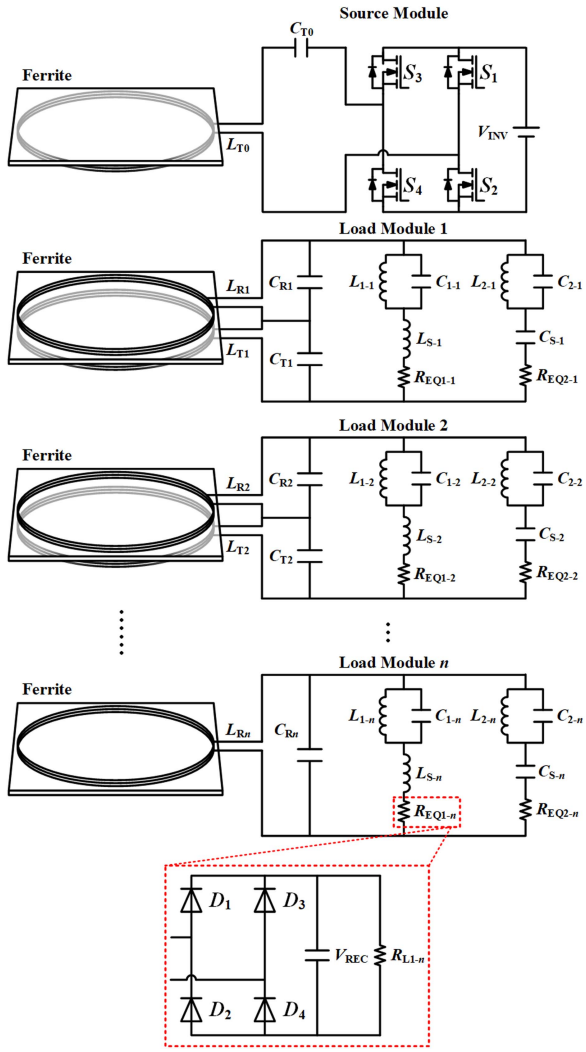

Fig. 2. Proposed dual-frequency WPT system with multiple CC outputs.

into two parts: the power module and the load modules. The power module consists of a dc voltage source with its dc voltage denoted as V_{INV}, an inverter consisting of four power MOSFETs S_1–S_4, a transmitting coil L_{T0}, and its compensation capacitor C_{T0}. The load module i ($i = 1, 2, \ldots, n$) consists of a receiving coil L_{Ri}, a transmitting coil L_{Ti}, the compensation capacitors C_{Ri}, C_{Ti}, band-stop filter network $L_{1\text{-}i}$, $L_{2\text{-}i}$, $L_{\mathrm{S}\text{-}i}$, $C_{1\text{-}i}$, $C_{2\text{-}i}$, $C_{\mathrm{S}\text{-}i}$, and the loads $R_{\mathrm{EQ1}\text{-}i}$, $R_{\mathrm{EQ2}\text{-}I}$, $R_{\mathrm{EQ1}\text{-}i}$, and $R_{\mathrm{EQ2}\text{-}i}$ are the ac equivalent model of a full bridge rectifier, a capacitor, and a load resistor that simplifies the analysis. Most of the components in the load modules have the same parameters for modularity

$$\begin{cases} L = L_{T0} = L_{R1} = L_{T1} = L_{Ri} = L_{Ti} \\ L_1 = L_{1-1} = L_{1-2} = L_{1-i} \\ L_2 = L_{2-1} = L_{2-2} = L_{2-i} \\ C = C_{T0} = C_{R1} = C_{T1} = C_{Ri} = C_{Ti} \quad (i = 1, 2, \ldots, n). \\ C_1 = C_{1-1} = C_{1-2} = C_{1-i} \\ C_2 = C_{2-1} = C_{2-2} = C_{2-i} \\ M = M_{01} = M_{12} = M_{(i-1)i} = kL \end{cases} \tag{1}$$

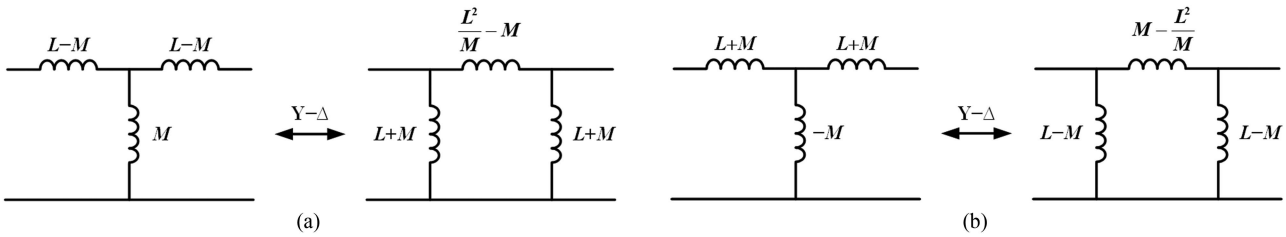

Fig. 3. T- and π-type decoupling equivalent circuits. (a) Positive coupled case. (b) Negative coupled case.

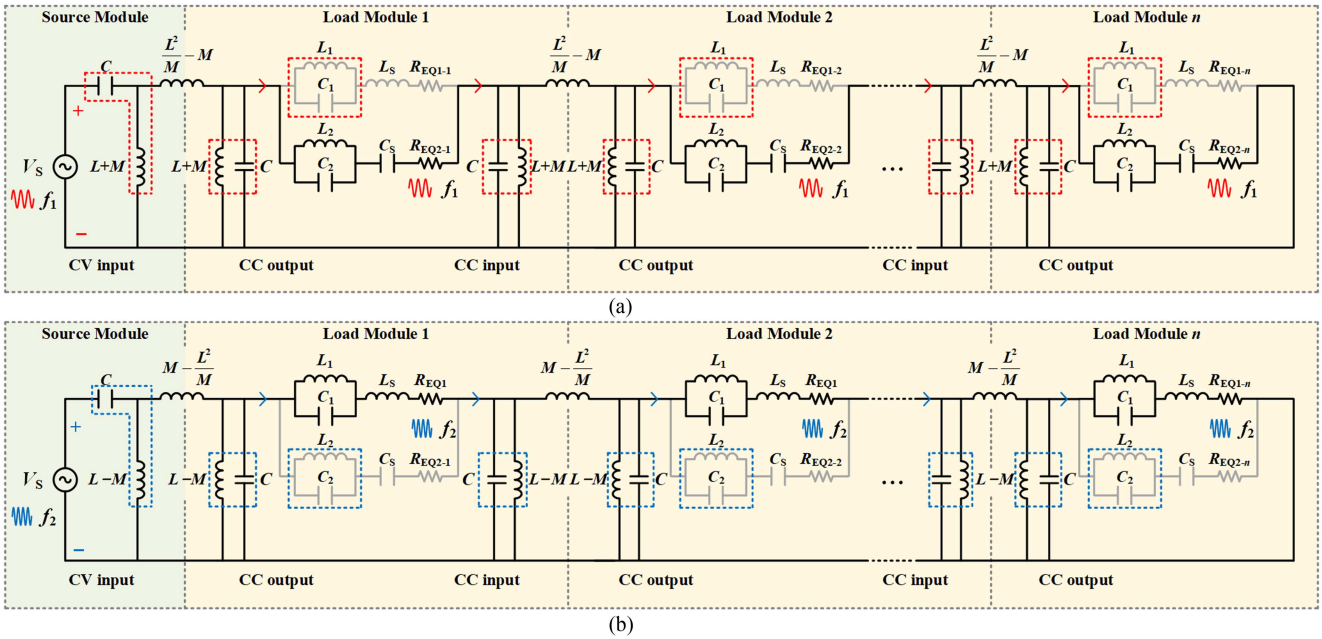

Fig. 4. Decoupling equivalent circuits. (a) At frequency f_1. (b) At frequency f_2.

The proposed WPT system is analyzed using the decoupling equivalent circuit and the fundamental harmonics approximation method. The RMS value of the inverter ac voltage V_S, the rectifier ac voltage V_R, and the equivalent ac load resistance R_{EQ} can be expressed as

$$V_S = \frac{2\sqrt{2}}{\pi} V_{\mathrm{INV}}, V_R = \frac{2\sqrt{2}}{\pi} V_{\mathrm{REC}}, R_{\mathrm{EQ}} = \frac{8}{\pi^2} V_L. \quad (2)$$

A. Dual-Frequency Resonant Topology

Four basic compensation topologies are widely used by WPT systems: series-series (S–S); series-parallel (S–P); parallel-series (P–S); and parallel-parallel (P–P). Each of these compensation topologies has a resonant frequency, f_0, which depends on the circuit parameters

$$f_0 = \frac{1}{2\pi\sqrt{LC}}. \quad (3)$$

When the operating frequency of the system f_S is equal to the resonant frequency, the input impedance of the system is resistive. However, as the operating frequency deviates from the resonant frequency, the input impedance could be either inductive or capacitive. This leads to a corresponding alteration in the phase angle relationship of the currents passing through the transmitting and receiving coils, I_P and I_S. In the case of parallel topology on the secondary side, if f_S falls below f_0, I_P and I_S are in phase, and the coils are positively coupled. If f_S exceeds f_0, I_P and I_S are in the opposite phase, and the coil is negatively coupled. These characteristics will be reversed in the case of a series topology on the secondary side.

Then the decoupling equivalent circuit can be used to obtain dual operating frequencies, f_1 and f_2 ($f_1 < f_2$). The T-type decoupling equivalent circuit is commonly used, and the π-type decoupling equivalent circuit can be obtained based on the star-delta transformation, as shown in Fig. 3. The π-type decoupling equivalent circuit at dual operating frequencies is shown in Fig. 4.

In Fig. 4(a), when $(L+M)$ resonates with C, the compensation capacitor of source module and the equivalent inductor form an LC resonant cavity. A load-independent CC output characteristic can be obtained if the input is a CV source. The compensation capacitor of load modules and the equivalent inductor resonate in parallel and are equivalent to an open circuit. If the input has

a CC characteristic, the output still has a load-independent CC characteristic. The resonant frequency can be expressed as

$$f_1 = \frac{1}{2\pi\sqrt{(L+M)C}} = \frac{f_0}{\sqrt{1+k}}. \tag{4}$$

Similarly in Fig. 4(b), when $(L-M)$ resonates with C, an LC resonant cavity is constructed to transform the CV input into a CC output and the compensation capacitors of load modules resonate with the equivalent inductors to achieve CC characteristic transfer from input to output. The resonant frequency can be expressed as

$$f_2 = \frac{1}{2\pi\sqrt{(L-M)C}} = \frac{f_0}{\sqrt{1-k}}. \tag{5}$$

By cascading an S–P topology with multiple P–P topologies, a dual-frequency multiple CC outputs WPT system can be obtained. According to (4) and (5), the relationship between the dual resonant frequencies can be obtained as

$$f_2 = \sqrt{\frac{1+k}{1-k}} f_1. \tag{6}$$

B. Band-Stop Filter Design

In multifrequency WPT systems, band-stop filter networks are constructed to decouple the outputs of loads and to achieve selective power transfer. The band-stop filter consists of multiple inductor-capacitor parallel combinations and a series of passive components. For the m parallel combination, the network impedance exists with m positive real poles and $m+1$ positive real zeros. The positive poles are used to block unwanted frequency components, and the positive zeros are used to allow desired frequency components to pass without loss. In the dual-frequency system, only one parallel combination is required. As shown in Fig. 5(a), L_1 (L_2) and C_1 (C_2) are in parallel resonance (equivalent to open circuit) at frequency f_1 (f_2) to stop the f_1 (f_2) component and L_1 (L_2), C_1 (C_2), and $L_{\text{F-}LC}$ ($C_{\text{F-}LC}$) are in series resonance (equivalent to short circuit) at frequency f_2 (f_1) to allow the f_2 (f_1) component to power the loads behind the filter network. The network impedance can be expressed as

$$\begin{cases} G_1(f_1) = \left(j2\pi f_1 C_1 + \frac{1}{j2\pi f_1 L_1}\right) // \left(\frac{1}{j2\pi f_1 L_{\text{F-}LC}}\right) = 0 \\ Z_1(f_2) = j2\pi f_2 L_1 // \frac{1}{j2\pi f_2 C_1} + j2\pi f_2 L_{\text{F-}LC} = 0 \\ Z_2(f_1) = j2\pi f_1 L_2 // \frac{1}{j2\pi f_1 C_2} + \frac{1}{j2\pi f_1 C_{\text{F-}LC}} = 0 \\ G_2(f_2) = \left(j2\pi f_2 C_2 + \frac{1}{j2\pi f_2 L_2}\right) // (j2\pi f_2 C_{\text{F-}LC}) = 0 \end{cases}. \tag{7}$$

C. Realization of Zero Phase Angle (ZPA)

Because the operating frequency deviates from f_0, the input impedance of the system is inductive or capacitive and there is a large reactive power. The size of passive components needs to be increased to cope with the voltage and current stresses generated by reactive power. Moreover, the system cannot realize zero voltage switching in capacitive input impedance. One solution is to add passive components to make the system resistive and achieve ZPA, as shown in Fig. 5(b).

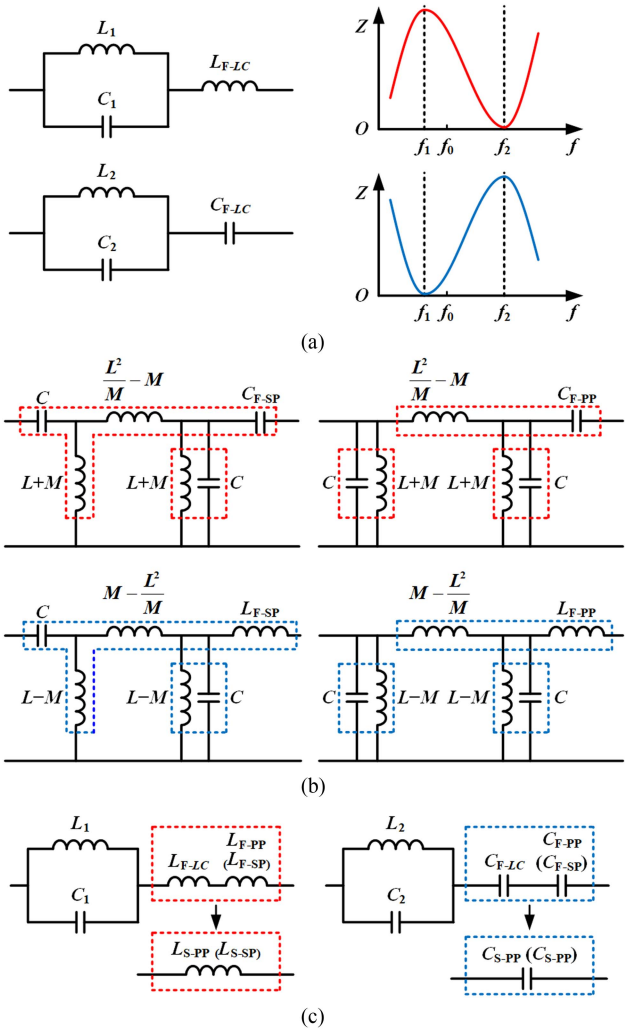

Fig. 5. Resonant states. (a) Band-stop filter. (b) Realization of zero phase angle for S–P topology and P–P topology. (c) Improvement of band-stop filters to realize ZPA.

For the S–P topology, the LC resonant cavity needs to be made into a T-type network so that the input impedance is resistive. The parameters of the passive components need to satisfy the following equations:

$$j2\pi f_1\left(\frac{L^2}{M} - M\right) + j2\pi f_1(L+M) + \frac{1}{j2\pi f_1 C_{\text{F-SP}}} = 0 \tag{8}$$

$$j2\pi f_2\left(M - \frac{L^2}{M}\right) + j2\pi f_2(L-M) + j2\pi f_2 L_{\text{F-SP}} = 0. \tag{9}$$

For the P–P topology, only the equivalent inductor needs to be compensated. The parameters of the passive components need to satisfy the following equations:

$$j2\pi f_1\left(\frac{L^2}{M} - M\right) + \frac{1}{j2\pi f_1 C_{\text{F-PP}}} = 0 \tag{10}$$

$$j2\pi f_2\left(M-\frac{L^2}{M}\right)+j2\pi f_2 L_{\text{F-PP}}=0. \tag{11}$$

At f_1, a capacitor needs to be added, while at f_2, it is an inductor. It cannot hold at the same time. As shown in Fig. 4, the components in series with the band-stop filter are only effective in the equivalent circuit at one frequency. Therefore, connecting the compensation components in series with the band-stop filter network avoids the effect on the input impedance at another frequency. Furthermore, the compensation components can be combined with a part of the filter network to reduce the number of passive components, as shown in Fig. 5(c). The mathematical relationship can be expressed as

$$\begin{cases} C_{\text{S-SP}}=\dfrac{1}{\frac{L}{MC}+\frac{L_2}{(L+M)C-L_2C_2}} \\ C_{\text{S-PP}}=\dfrac{1}{\frac{L-M}{MC}+\frac{L_2}{(L+M)C-L_2C_2}} \end{cases} \tag{12}$$

$$\begin{cases} L_{\text{S-SP}}=\dfrac{L^2}{M}-L+\dfrac{L_1}{(L-M)CL_1C_1-1} \\ L_{\text{S-PP}}=\dfrac{L^2}{M}-M+\dfrac{L_1}{(L-M)CL_1C_1-1} \end{cases}. \tag{13}$$

The parameters of the load submodule are

$$\begin{cases} C_{\text{S-1}}=C_{\text{S-SP}} \\ L_{\text{S-1}}=L_{\text{S-SP}} \\ C_{\text{S-2}}=C_{S-3}=\ldots=C_{S-n}=C_{\text{S-PP}} \\ L_{\text{S-2}}=L_{S-3}=\ldots=L_{S-n}=L_{\text{S-PP}} \end{cases}. \tag{14}$$

D. Operating Modes

Correspondingly, the system has three operating modes.

1) *Mode 1:* The inverter operates at the switching frequency f_1, supplying power to the loads $R_{\text{EQ2-1}}$, $R_{\text{EQ2-2}},\ldots,$ $R_{\text{EQ2-}n}$.
2) *Mode 2:* The inverter operates at the switching frequency f_2, supplying power to the loads $R_{\text{EQ1-1}}$, $R_{\text{EQ1-2}},\ldots,$ $R_{\text{EQ1-}n}$.
3) *Mode 3:* One arm of the inverter operates at the switching frequency f_1 and the other at f_2.

The output currents in Mode 1 can be expressed as

$$\begin{cases} I_{RL1\text{-}1}=I_{RL1\text{-}2}=\cdots=I_{RL1-n}=0 \\ I_{RL2\text{-}1}=I_{RL2\text{-}2}=\cdots=I_{RL2-n}=\frac{8}{\pi^2}\frac{V_{INV}}{j2\pi f_1(L+M)} \end{cases} \tag{15}$$

The output currents in mode 2 can be expressed as

$$\begin{cases} I_{RL1\text{-}1}=I_{RL1\text{-}2}=\cdots=I_{RL1-n}=\frac{8}{\pi^2}\frac{V_{INV}}{j2\pi f_2(L-M)} \\ I_{RL2\text{-}1}=I_{RL2\text{-}2}=\cdots=I_{RL2-n}=0 \end{cases}. \tag{16}$$

The output currents in mode 3 can be expressed as

$$\begin{cases} I_{RL1\text{-}1}=I_{RL1\text{-}2}=\cdots=I_{RL1-n}=\frac{4}{\pi^2}\frac{V_{INV}}{j2\pi f_2(L-M)} \\ I_{RL2\text{-}1}=I_{RL2\text{-}2}=\cdots=I_{RL2-n}=\frac{4}{\pi^2}\frac{V_{INV}}{j2\pi f_1(L+M)} \end{cases}. \tag{17}$$

The system efficiency η can be defined as

$$\eta=\frac{P_{\text{out}}}{P_{\text{in}}}=\frac{\sum\left(I_{\text{RL1}-i}^2R_{\text{L1}-i}+I_{\text{RL2}-i}^2R_{\text{L2}-i}\right)}{V_{\text{INV}}I_{\text{dc}}}. \tag{18}$$

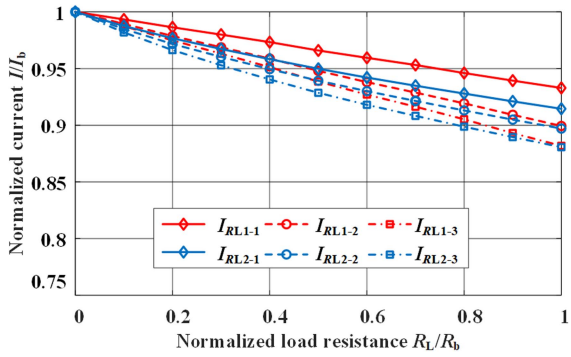

Fig. 6. Output variations against the load resistances ($k=0.4$, $Q_a=Q_b=200$).

III. Power Transfer Capability Analysis

A. Impact of Parasitic Resistances

The above analyses are based on the ideal case where the parasitic resistance is zero. In practical systems, parasitic resistance cannot be ignored, destroying the CC output characteristics. The quality factors of L_{Ti}, L_{Ri}, $L_{1\text{-}i}$, $L_{2\text{-}i}$, and L_{Si} at f_1 frequency are defined as $Q_{\text{T}i}$, $Q_{\text{R}i}$, $Q_{1\text{-}i}$, $Q_{2\text{-}i}$, and Q_{Si}. The parasitic resistance can be expressed as

$$r_i=2\pi f_1L_i/Q_i. \tag{19}$$

Considering that the inductors have different roles in the system, transmission coils and compensation inductors, Q can be divided into Q_a and Q_b correspondingly. $Q_{Ti}=Q_{Ri}=Q_a$; $Q_{1\text{-}i}=Q_{2\text{-}i}=Q_b$. The parasitic resistance of L_S is in series with the load and is much smaller than the load, so its effect is negligible.

A simulation model with three load modules was built, and the trend of output current for different load resistances is shown in Fig. 6. I_b is the output current ignoring parasitic resistances. Due to the presence of parasitic resistance, the output current decreases as the loads increase and $I_{RL1\text{-}i}$ ($I_{RL2\text{-}i}$) is larger than $I_{RL1\text{-}(i+1)}$ ($I_{RL2\text{-}(i+1)}$) in different load modules. With a large load resistance and numerous submodules, the output power is at the risk of significant reduction.

The output variations against the coupling coefficient and quality factor can be seen in Fig. 7. The current is normalized by dividing the minimum value by the maximum value within the range of load resistances. The fluctuation of output current increases with decreasing quality factor Q_a, while Q_b has almost no effect on the output variation. The increase in the coupling coefficient k reduces the output current variation, so higher coupling coefficients can be taken at low-quality factor Q_a to mitigate the output fluctuation. In summary, a higher quality factor Q_a and a higher coupling coefficient k are preferred in parametric design.

B. Parameters Tolerance

Fig. 8 shows the output fluctuations against the mutual inductance. Outputs are well stabilized over a range of plus or minus 2%. Fig. 9 shows the output fluctuations against the inductance

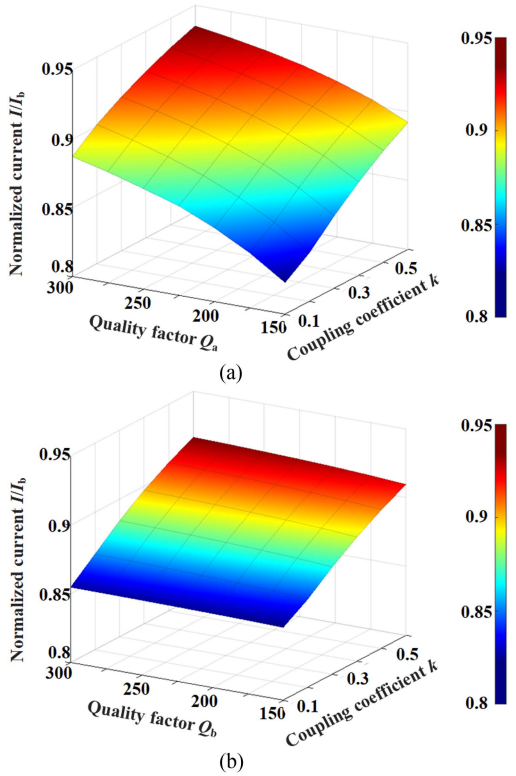

Fig. 7. Output variations against coupling coefficient k. (a) With varying quality factor Q_a ($Q_b = 200$). (b) With varying quality factor Q_b ($Q_a = 200$).

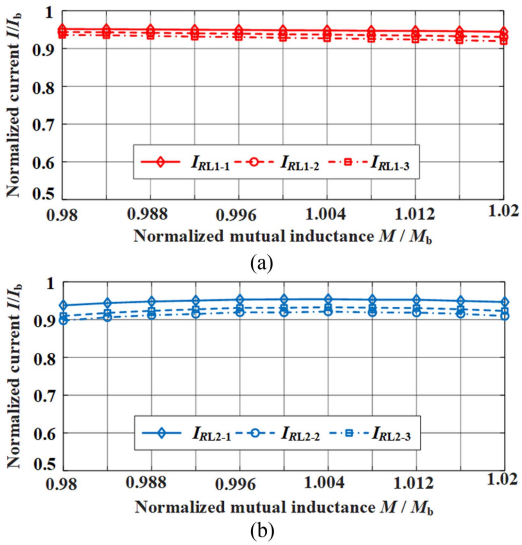

Fig. 8. Output fluctuations against the mutual inductance. (a) At f_2. (b) At f_1.

L_R and L_T. Besides the deviation of mutual inductance from its original value, the deviation of transmission coil self-inductance affects the outputs. As the normalized self-inductance L_R goes from 0.98 to 1.02, the output related to frequency f_1 gradually decreases, while the output related to frequency f_2 gradually increases. Moreover, the outputs of the rear submodule are more

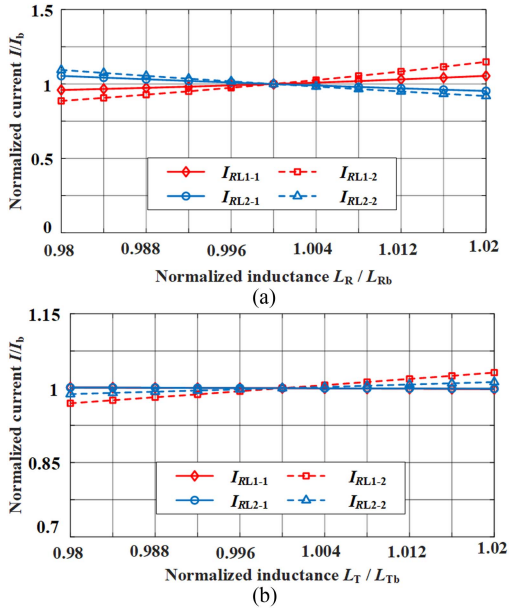

Fig. 9. Output fluctuations against the self-inductance. (a) Normalized L_R. (b) Normalized L_T.

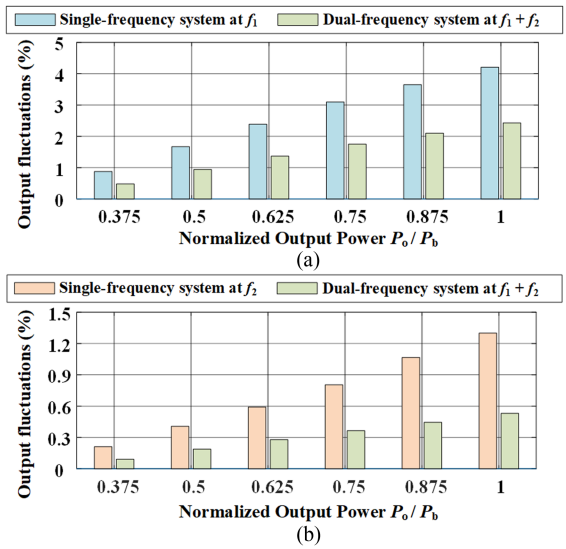

Fig. 10. Output fluctuations of proposed dual-frequency system vs. single-frequency system. (a) At f_1. (b) At f_2.

affected. As a comparison, the outputs are less affected when the L_T is changed.

C. Output Fluctuations

Fig. 10 shows the output fluctuations of proposed dual-frequency system and single-frequency system. For a better comparison of the ability of different topologies to suppress output fluctuations, it is set that the comparison is performed at the same output power. P_b is the rated output power. The load current varies with the load, and there is no definite reference value for evaluating the CC output. Define the rate of fluctuation

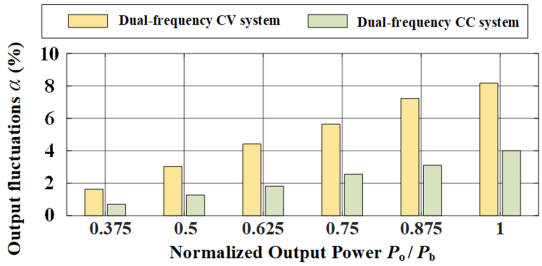

Fig. 11. Output fluctuations of proposed dual-frequency CC system vs. dual-frequency CV system.

of the output current as

$$\alpha = \frac{I_{\text{OUT\_MAX}} - I_{\text{OUT\_MIN}}}{I_{\text{OUT\_MAX}} + I_{\text{OUT\_MIN}}} \times 100\%. \tag{20}$$

In proposed dual-frequency system, the loads corresponding to each frequency contribute half of the output power. At the frequency f_1, the output fluctuations of single-frequency system and dual-frequency system are 4.21% and 2.42%. The absolute reduction percentage is less than 2%. Considering the original fluctuation of 4.21%, this improvement is significant. Also, the smallest output normalized current, which happens at the last stage and at rated output, is increased from 0.872 to 0.963. The improvement is 10.43%. The output fluctuations are 1.30% and 0.53% at the frequency f_2. It shows that the dual-frequency system has better characteristics in resisting output fluctuations. As shown in Fig. 6, the outputs decrease with increasing power. Higher output power means higher output fluctuations. Thanks to the band-stop filter design, the dual-frequency system can be seen as a superposition of two mutually independent single-frequency systems. Each single-frequency system is responsible for half of the output power, which means lower output fluctuations.

Fig. 11 shows the output fluctuations of dual-frequency system with CC outputs and the dual-frequency system with CV outputs. The same system parameters are employed in both the CC and CV systems, except for the compensation inductor L_S and the compensation capacitor C_S. The power distribution is configured as described before. The maximum output fluctuations of CV system and CC system are 8.17% and 4.00%. Due to the circuit topology of the CC system, the effect of parasitic resistance on the outputs is minimized.

IV. Magnetic Couplers

The proposed magnetic couplers are shown in Fig. 12. Similar to the circuit topology, there are also two types of couplers corresponding to the power modules and load modules. The coupler of the power module is simply composed of a ferrite plate and a bipolar coil. In contrast, the coupler of the load modules comprises multiple coils. The couplers are with a size of 200 × 200 mm. The transfer distance is 40 mm. To avoid the use of discrete inductors, compensation inductors are integrated into the coupler to increase power density.

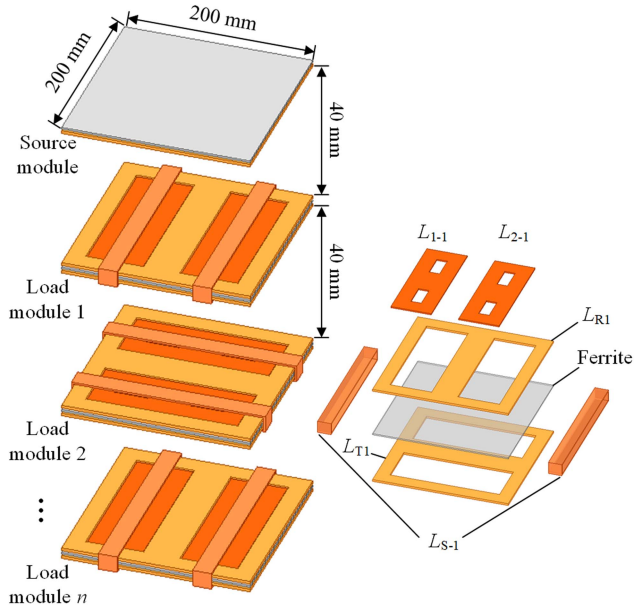

Fig. 12. Proposed magnetic couplers.

TABLE I
Coupling Coefficient Matrix

k	L_T	L_R	L_1	L_2	L_S
L_T	1	0.0056	0.0091	0.0076	0.0011
L_R	0.0056	1	0.0040	0.0005	0.0094
L_1	0.0091	0.0040	1	0.0037	0.0018
L_2	0.0076	0.0005	0.0037	1	0.0005
L_S	0.0011	0.0094	0.0018	0.0005	1

There are three typical methods used for decoupling design in WPT systems. The first method is magnetic field cancellation. The physical definition of the mutual inductance is the ratio of the mutual flux linkage to the current. Therefore, when the mutual flux is zero, the mutual inductance goes to zero and the coils become decoupled. Take the decoupling of the bipolar coils along different axes as an example. When the two coils completely overlap, one half of the flux is positive and the other half is negative. The two components are equal and opposite. The sum of the mutual magnetic flux is zero and the two coils realize decoupling. L_T, L_R, L_1, and L_2 are designed as bipolar coils placed along different directions. Thus, the load modules are placed in a rotation of 90 degrees along the center axis in sequence. The coupling between L_1, L_2, and L_T relies on ferrite for shielding. The second approach is that coils are arranged at a sufficient distance to eliminate the cross-coupling, like L_1 and L_2. The last method is using solenoid coils. The magnetic field direction of the solenoid coil is spatially orthogonal to that of the planar coil, and there is no cross-linking of the magnetic flux, which naturally decouples the coils. L_S is designed as a solenoid coil. The L_S is divided into two parts placed on both sides of the coupler with the currents in opposite directions.

The cross-coupling of different coils is given in Table I. All the values of cross-coupling are small enough to lie within the range that can be considered decoupled ($|k| < 0.01$). Considering

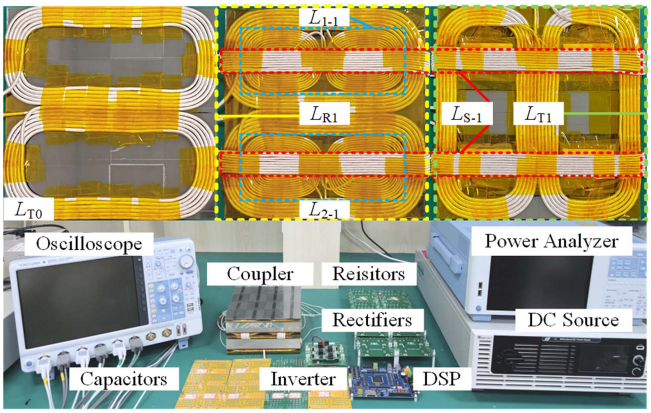

Fig. 13. Photograph of the experimental setup.

TABLE II
PARAMETERS OF EXPERIMENTAL SETUP

Symbol	Value	Symbol	Value	Symbol	Value
V_{INV}	45 V	f_1	200 kHz	f_2	306.1 kHz
R_L	25~75 Ω	L_{T0}	35.67 μH	L_{T1}	35.89 μH
L_{R1}	35.57 μH	L_{R2}	36.23 μH	M_{01}	14.26 μH
M_{12}	14.25 μH	$L_{1\text{-}1}$	21.38 μH	$L_{2\text{-}1}$	22.03 μH
$L_{1\text{-}2}$	22.23 μH	$L_{2\text{-}2}$	22.55 μH	$L_{S\text{-}1}$	69.45 μH
$L_{S\text{-}2}$	91.72 μH	C_{T0}	12.90 nF	C_{T1}	12.70 nF
C_{R1}	12.835 nF	C_{R2}	12.573 nF	$C_{1\text{-}1}$	30.906 nF
$C_{2\text{-}1}$	12.594 nF	$C_{1\text{-}2}$	29.203 nF	$C_{2\text{-}2}$	12.370 nF
$C_{S\text{-}1}$	4.017 nF	$C_{S\text{-}2}$	5.490 nF		

the current withstand capability of the coil, system efficiency, and output current fluctuation, the turns of L_T, L_R, L_1, and L_2 are set to 6, 6, 12, and 12, respectively. The turns of L_S are 9 and 11 in the case of $L_{S\text{-}SP}$ and $L_{S\text{-}PP}$, respectively.

V. EXPERIMENTAL VERIFICATION

A power relay system containing two load modules is built, as shown in Fig. 13, and the parameters of the experimental setup are given in Table II. All the coils were wound from Litz wires to get high-quality factors. The signals are generated by a digital signal processor TMS320F28335. The system is powered by the bidirectional dc power supply Chroma 62180D. The input, the outputs, and the efficiency are measured by precision power analyzers Yokogawa WT5000. To verify the feasibility of selective CC output in various cases, the following experiments are designed.

1) $R_{L1\text{-}1}$ and $R_{L1\text{-}2}$ are varied from 25 to 75 Ω, other loads are fixed at 25 Ω.
2) $R_{L2\text{-}1}$ and $R_{L2\text{-}2}$ are varied from 50 to 100 Ω, other load are fixed at 25 Ω.

In mode 1, $R_{L1\text{-}1}$ and $R_{L1\text{-}2}$ are not powered, and the load variation is meaningless, which can be discarded. $R_{L2\text{-}1}$ and $R_{L2\text{-}2}$ in mode 2 are the same. Thus, these two situations are not discussed.

The output current variations in each mode are shown in Figs. 14 and 15. In mode 1, when $R_{L2\text{-}1}$ and $R_{L2\text{-}2}$ are varied from 25 to 75 Ω with the others assigned to 25 Ω, $I_{RL2\text{-}1}$ decreased from 0.541 to 0.511 A and $I_{RL2\text{-}2}$ decreased from 0.497 to 0.467 A. α is 2.851% and 3.134%. In contrast, the maximum of $I_{RL1\text{-}1}$ and $I_{RL1\text{-}2}$ is 0.038 A, significantly lower than the output currents. Similarly, in mode 2, when $R_{L1\text{-}1}$ and $R_{L1\text{-}2}$ are varied from 50 to 100 Ω with the others assigned to 25

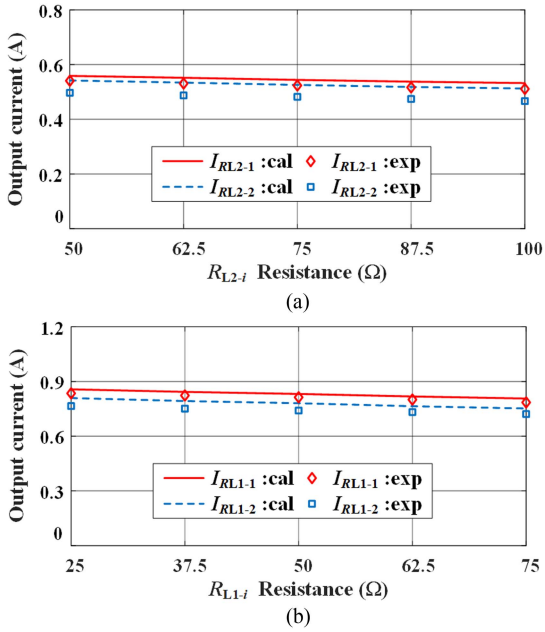

Fig. 14. Output current variations. (a) Mode 1. (b) Mode 2.

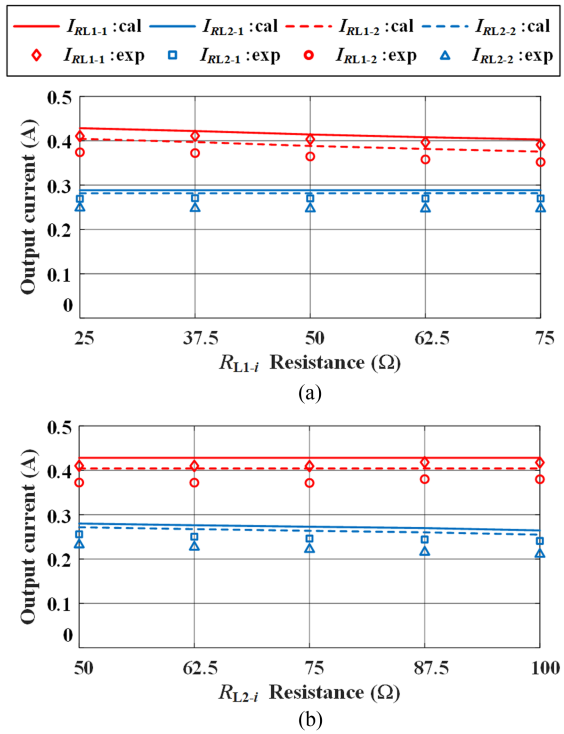

Fig. 15. Output current variations in Mode 3. (a) Varying $R_{L1\text{-}i}$. (b) Varying $R_{L2\text{-}i}$.

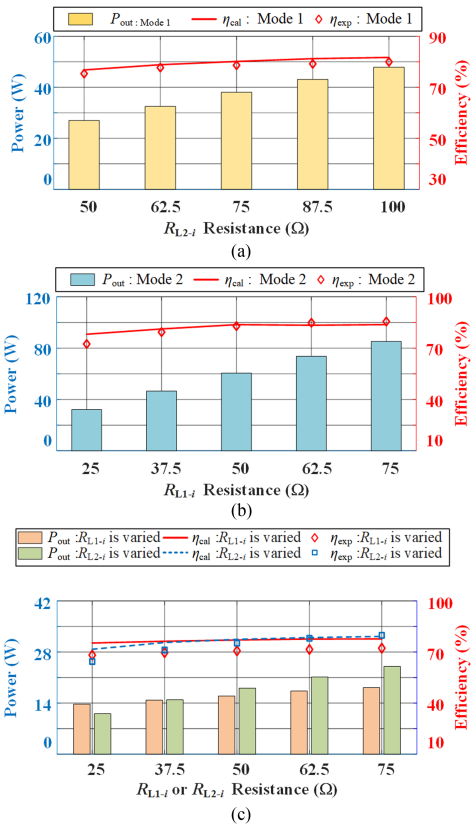

Fig. 16. Output power and efficiency. (a) Mode 1. (b) Mode 2. (c) Mode 3.

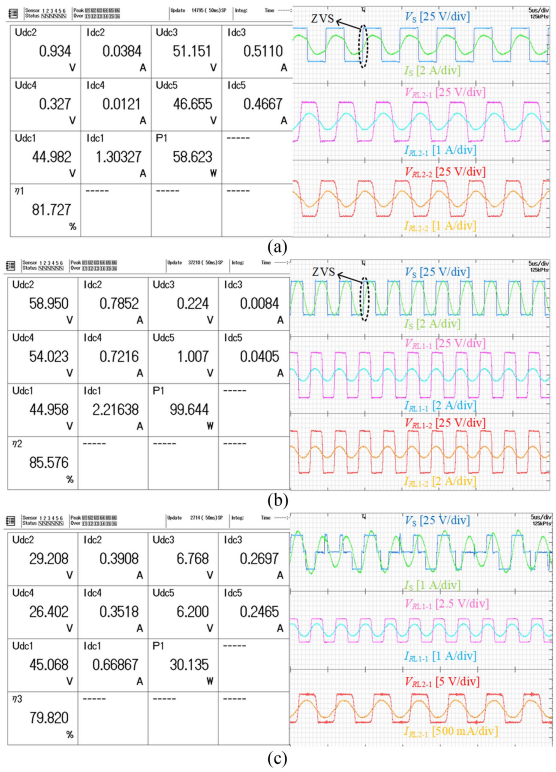

Fig. 17. Experimental waveforms of the inverter output and loads. (a) Mode 1. (b) Mode 2. (c) Mode 3.

Ω, $I_{RL1\text{-}1}$ decreased from 0.835 to 0.785 A and $I_{RL1\text{-}2}$ decreased from 0.766 to 0.722 A. α is 3.080% and 2.952%. The maximum of $I_{RL2\text{-}1}$ and $I_{RL2\text{-}2}$ is 0.041 A. The system can achieve selective power transfer by switching between the different modes. $I_{RL2\text{-}1}$ and $I_{RL2\text{-}2}$ are unaffected by the variation of $R_{L1\text{-}1}$ and $R_{L1\text{-}2}$, as shown in Fig. 15(a). Similarly, $I_{RL1\text{-}1}$ and $I_{RL1\text{-}2}$ are unaffected by the variation of $R_{L2\text{-}1}$ and $R_{L2\text{-}2}$, as shown in Fig. 15(b). Overall, the maximum α of the system is 4.78%, and most of the output current fluctuations are less than 3%, which is an acceptable value.

Fig. 16 shows the system efficiency and output power for each experiment group. It is easily obtained that the system can achieve a maximum efficiency of 85.58% and a maximum output power of 99.64 W, which is qualified as an auxiliary power supply. Fig. 17 shows the experimental waveforms of the inverter output and loads. In Fig. 17(c), the waveforms of $R_{L1\text{-}1}$ contain only frequency f_2 components, and the waveforms of $R_{L2\text{-}1}$ contain only frequency f_1 components so that the filter networks can handle the unwanted frequency components as well as the harmonic components from the inverter well.

VI. Conclusion

A multioutput WPT system with CC characteristics has been proposed in this article for auxiliary power supply in medium- and high-capacity power applications. CC output in dual frequencies is achieved using S–P topology and P–P topology. Passive components are added to compensate for reactive power and to avoid the failure of soft switching. The band-stop filter network allows the system to control the power distribution flexibly. Various decoupling methods are used to integrate the compensation inductors into the coupler. A WPT system containing two load modules is constructed, and the experiments demonstrate that the proposed system can achieve high efficiency and multiple decoupled CC characteristic outputs.

References

[1] C. Cai et al., "Robust wide-area wireless charging of multipath movable receivers: A coupling mechanism and simplified configuration strategy," *IEEE Trans. Power Electron.*, vol. 40, no. 1, pp. 2527–2541, Jan. 2025, doi: 10.1109/TPEL.2024.3446788.

[2] Y. Zhang, H. Zhou, Z. Shen, R. Xie, X. Chen, and X. Mao, "An interoperable dynamic wireless charging system with stable output based on a self-adaptive two-pole receiver," *IEEE Trans. Power Electron.*, vol. 39, no. 10, pp. 11943–11947, Oct. 2024.

[3] E. Rong, P. Sun, G. Yang, J. Xia, Z. Liu, and S. Li, "5-kW, 96.5% efficiency capacitive power transfer system with a five-plate coupler: Design and optimization," *IEEE Trans. Power Electron.*, vol. 40, no. 1, pp. 2542–2555, Jan. 2025, doi: 10.1109/TPEL.2024.3462410.

[4] W. Pan, C. Liu, H. Tang, Y. Zhuang, and Y. Zhang, "An interoperable electric vehicle wireless charging system based on mutually spliced double-D coil," *IEEE Trans. Power Electron.*, vol. 39, no. 3, pp. 3864–3872, Mar. 2024.

[5] T. Li et al., "Enhancing V2G applications: Analysis and optimization of a CC/CV bidirectional IPT system with wide range ZVS," *IEEE Trans. Transp. Electrific.*, to be published, doi: 10.1109/TTE.2024.3369079.

[6] H. Tang et al., "A self-adaptive dual-channel LCC-S detuned topology for misalignment tolerance in AUV wireless power transfer systems," *IEEE Trans. Power Electron.*, to be published, doi: 10.1109/TPEL.2024.3492194

[7] Y. Chen et al., "A clamp circuit-based inductive power transfer system with reconfigurable rectifier tolerating extensive coupling variations," *IEEE Trans. Power Electron.*, vol. 39, no. 2, pp. 1942–1946, Feb. 2024.

[8] Y. Zhang, H. Zhou, Z. Shen, R. Xie, Z. Zheng, and X. Chen, "A family of self-adaptive interoperable receivers based on multiple decoupled receiving poles for electric vehicle wireless charging systems," *IEEE Trans. Power Electron.*, vol. 39, no. 9, pp. 11794–11802, Sep. 2024.
[9] Y. Zhang, C. Liu, M. Zhou, and X. Mao, "A novel asymmetrical quadrupolar coil for interoperability of unipolar, bipolar, and quadrupolar coils in electric vehicle wireless charging systems," *IEEE Trans. Ind. Electron.*, vol. 71, no. 4, pp. 4300–4303, Apr. 2024.
[10] C. Liu, Y. Guan, Y. Wang, and D. Xu, "A multi-matrix based network for multi-module parallel megahertz inverter system," *IEEE Trans. Power Electron.*, vol. 39, no. 9, pp. 11308–11317, Sep. 2024, doi: 10.1109/TPEL.2024.3406470.
[11] O. C. Spro et al., "Optimized design of multi-MHz frequency isolated auxiliary power supply for gate drivers in medium-voltage converters," *IEEE Trans. Power Electron.*, vol. 35, no. 9, pp. 9494–9509, Sep. 2020.
[12] K. Sun, J. Wang, R. Burgos, D. Boroyevich, J. Stewart, and N. Yan, "Design and multiobjective optimization of an auxiliary wireless power transfer converter in medium-voltage modular conversion systems," *IEEE Trans. Power Electron.*, vol. 37, no. 8, pp. 9944–9958, Aug. 2022.
[13] X. Hou, H. Hu, Y. Su, Z. Liu, Z. Deng, and R. Deng, "A multirelay wireless power transfer system with double-sided LCC compensation network for online monitoring equipment," *IEEE J. Emerg. Sel. Top. Power Electron.*, vol. 11, no. 1, pp. 1262–1271, Feb. 2023.
[14] J.-H. Cho, S. Jung, and Y.-J. Kim, "Wireless power transfer for variable load, distance, and power division ratio in a loosely-coupled multiple-receiver relay system," *IEEE Trans. Ind. Electron.*, vol. 70, no. 7, pp. 6809–6818, Jul. 2023.
[15] C. Cheng, X. Zheng, Y. Zhang, and W. Hua, "Load-independent class-E inverter with dual quasi-constant outputs," *IEEE Trans. Power Electron.*, vol. 39, no. 10, pp. 14015–14026, Oct. 2024, doi: 10.1109/TPEL.2024.3420809.
[16] X. Li, F. Zheng, H. Wang, X. Dai, Y. Sun, and J. Hu, "Analysis and design of a cost-effective single-input and regulatable multioutput WPT system," *IEEE Trans. Power Electron.*, vol. 38, no. 6, pp. 6939–6944, Jun. 2023.
[17] C. Zhu, X. He, Y. Gu, B. Yang, Y. Chen, and R. Mai, "Analysis and design of multiple regulatable output rectifier-integrated buck converter for wireless power transfer application," *IEEE Trans. Power Electron.*, vol. 39, no. 8, pp. 9138–9143, Aug. 2024.
[18] W. Chen, K. Ji, Y. Zhang, and J. Wang, "Design and analysis of multiload inductive power transfer system using bilateral-excitation scheme," *IEEE Trans. Ind. Electron.*, vol. 18, no. 1, pp. 365–374, Jan. 2022.
[19] C. Xia, Y. Chen, A. Sun, Y. Cao, X. Wang, and Q. Wang, "Switching frequency control strategy of inverter for multifrequency multiload WPT system based on hysteresis current control," *IEEE Trans. Power Electron.*, vol. 39, no. 10, pp. 13946–13961, Oct. 2024, doi: 10.1109/TPEL.2024.3416671.
[20] W. Xiong, F. Jiang, Z. Liu, Q. Zhu, and M. Su, "A hybrid-frequency-based multi-load wireless power transfer system with constant current or voltage outputs," *IEEE J. Emerg. Sel. Top. Power Electron.*, vol. 12, no. 1, pp. 1150–1160, Feb. 2024.
[21] W. Pan et al., "A dual-frequency modular wireless power transfer system for auxiliary power supply of power electronics converters," *IEEE Trans. Power Electron.*, vol. 39, no. 9, pp. 11814–11823, Sep. 2024.

Wenxuan Pan was born in Shanxi, China. He is currently working toward the master's degree in power electronics with the School of Electrical Engineering and Automation, Fuzhou University, Fuzhou, China.

His research direction includes wireless power transfer.

Rongbin Liu was born in Fujian, China. He is currently working toward the master's degree in electrical engineering with the School of Electrical Engineering and Automation, Fuzhou University, Fuzhou, China.

His research direction includes wireless power transfer.

Ronghuan Xie (Graduate Student Member, IEEE) was born in Fujian, China. He is currently working toward the master's degree in electrical engineering with the School of Electrical Engineering and Automation, Fuzhou University, Fuzhou, China.

His research direction includes wireless power transfer.

Yizhan Zhuang (Member, IEEE) was born in Fujian, China, in 1994. He received the B.S. degree in electrical engineering from the College of Electrical Engineering and Automation, Fuzhou University, Fuzhou, China, in 2017, and the Ph.D. degree in electrical engineering from the School of Electrical Engineering, Wuhan University, Wuhan, China, in 2023.

He is currently a Lecturer (Associate Researcher) with the School of Electrical Engineering and Automation, Fuzhou University, Fuzhou, China. His research interests include dc–dc power converter and interface of photovoltaic conversion systems.

Xingkui Mao (Member, IEEE) received the B.E. and Ph.D. degrees in electrical engineering from Fuzhou University, Fuzhou, China, in 2000 and 2006, respectively.

He is currently a Professor with the College of Electrical Engineering and Automation, Fuzhou University. His research interests include design, manufacturing, and control for power electronic systems and components.

Yiming Zhang (Senior Member, IEEE) received the B.S. and Ph.D. degrees in electrical engineering from Tsinghua University, Beijing, China, in 2011 and 2016, respectively.

Afterwards, he was a Postdoctoral Researcher with San Diego State University, San Diego, CA, USA and a Research Fellow with Nanyang Technological University, Singapore. He is currently a Full Professor with Fuzhou University. He has authored 1 book from Springer, authored or co-authored more than 100 technical papers in journals and conference proceedings. His research interests include wireless power transfer and resonant converters.

Dr. Zhang was the recipient of the Outstanding Doctoral Dissertations of Tsinghua University in 2016. He was recognized as an Outstanding Reviewer for IEEE TRANSACTIONS ON POWER ELECTRONICS in 2019 and 2022, and a Distinguished Reviewer for IEEE TRANSACTIONS ON INDUSTRIAL ELECTRONICS in 2020. He was the Publication Chair of the international conference ICWPT2022.